

<https://doi.org/10.1038/s43246-025-00936-7>

# Imaging magnetic order in a two-dimensional iron-rich phyllosilicate



Muhammad Zubair Khan<sup>1,9</sup>, Andriani Vervelaki<sup>2,9</sup>, Daniel Jetter<sup>2,9</sup>, Kousik Bagani<sup>2,9</sup>, Andreas Ney<sup>3</sup>, Oleg E. Peil<sup>4</sup>, Sergio Valencia<sup>5</sup>, Alevtina Smekhova<sup>5</sup>, Florian Kronast<sup>5</sup>, Daniel Knez<sup>6</sup>, Martina Dienstleder<sup>7</sup>, Martino Poggio<sup>2,8</sup> ✉ & Aleksandar Matković<sup>1</sup> ✉

Magnetic domain formation in two-dimensional materials offers insight into the fundamentals of magnetism and serves as a catalyst for the advancement of spintronics. In order to propel these developments, it is crucial to acquire an understanding of the evolution of magnetic ordering at the nanometer scale. In particular, two-dimensional magnetic insulators allow for the realization of atomically sharp magnetoresistive tunneling junctions with nonmagnetic electrodes, therefore lifting one of the major constraints for the realization of computing in memory based on magnetoresistive elements. In this study, we visualize magnetic ordering in monolayers of annite, a fully air-stable layered magnetic mica. Using a nanometer-scale scanning superconducting quantum interference device microscopy, we directly observe domain formation in this representative of two-dimensional magnetic phyllosilicates.

Two-dimensional (2D) magnets are an exceptionally rich class of materials both for studying the fundamentals of magnetism and for potential applications in spintronics<sup>1–5</sup>. The van der Waals (vdW) nature of these materials makes them interesting to study because it covalently decouples them from the substrate and achieves a closer to ideal 2D limit, compared to conventional magnetic thin films or substrate/interface mediated magnetism<sup>6</sup>. In particular, 2D magnetic insulators are interesting for integration into tunnel junctions, where the presence of the external magnetic field can be used to modulate the tunneling barrier<sup>7</sup>. Their integration into metal-insulator-metal junctions could open avenues for developing low-power and high-efficiency electronic devices, magnetoresistive memory, and self-reconfiguring circuits<sup>8</sup>. Using 2D magnetic insulators lifts the need for ferromagnetic electrodes, and their vdW nature enables atomically sharp interfacing. Consequently, memory elements based on 2D magnetic insulators could be closely integrated with logic devices, as diffusion of magnetic ions is not an issue<sup>9</sup>.

To date, monolayers of FePS<sub>3</sub><sup>10,11</sup>, CrPS<sub>4</sub><sup>12</sup>, CrSBr<sup>13</sup>, CrI<sub>3</sub><sup>14</sup>, Cr<sub>2</sub>Ge<sub>2</sub>Te<sub>6</sub><sup>15</sup> and Fe<sub>3</sub>GeTe<sub>2</sub><sup>16</sup> are among the most extensively investigated 2D magnetic systems. Ordering in their atomically thin films can be efficiently modulated by external stimuli, such as electric and magnetic field<sup>17–19</sup>. Many 2D magnets exhibit A-type layer-by-layer antiferromagnetic ordering and consequently, e.g., thin films of CrI<sub>3</sub> and CrPS<sub>4</sub> with an odd number of

mono-layers have a net moment due to an uncompensated layer<sup>12,14,20</sup>. To image magnetic domains in 2D layer-dependent magnetic systems, a range of scattering techniques has been employed, including magneto-optical Kerr effect, x-ray magnetic circular dichroism, and neutron scattering<sup>14,21–23</sup>.

From an implementation perspective, 2D vdW magnets face challenges related to ambient stability<sup>24,25</sup>, necessitating encapsulation during fabrication and limiting their potential applications. One promising alternative involves alloying transition metal dichalcogenide monolayers with magnetic elements like V, Fe, or Co<sup>26–28</sup>, or synthesizing 2D silica thin films incorporating transition metal cations<sup>29,30</sup>. However, in both cases, ensuring low concentration and uniform distribution of these dopants is crucial for stabilizing the 2D magnetic structure.

Naturally occurring phyllosilicates offer air-stable layered structures with diverse compositions and an opportunity to integrate high concentrations of magnetic ions<sup>31,32</sup>. Recent studies on this class in the 2D limit have demonstrated that crystalline phyllosilicates retain large band gaps, high dielectric constant, and can incorporate magnetic moment ions and retain full ambient stability in monolayers, which are vital for future nanotechnology applications<sup>31–35</sup>. Due to their bio-compatibility and their capability for inter-layer ion exchange, they are also interesting candidates for cancer treatment<sup>36</sup>. With respect to nanotechnologies, talc was among the first phyllosilicates

<sup>1</sup>Chair of Physics, Department Physics, Mechanics and Electrical engineering, Montanuniversität Leoben, Leoben, Austria. <sup>2</sup>Department of Physics, University of Basel, Basel, Switzerland. <sup>3</sup>Institut für Halbleiter- und Festkörperphysik, Johannes Kepler Universität, Linz, Austria. <sup>4</sup>Group of computational materials design, Materials Center Leoben Forschung GmbH, Leoben, Austria. <sup>5</sup>Department of Spin and Topology in Quantum Materials, Helmholtz-Zentrum Berlin, Berlin, Germany. <sup>6</sup>Institute of Electron Microscopy and Nanoanalysis, Graz University of Technology (NAWI Graz), Graz, Austria. <sup>7</sup>Graz Centre for Electron Microscopy, Graz, Austria. <sup>8</sup>Swiss Nanoscience Institute, University of Basel, Basel, Switzerland. <sup>9</sup>These authors contributed equally: Muhammad Zubair Khan, Andriani Vervelaki, Daniel Jetter, Kousik Bagani. ✉ e-mail: [martino.poggio@unibas.ch](mailto:martino.poggio@unibas.ch); [aleksandar.matkovic@unileoben.ac.at](mailto:aleksandar.matkovic@unileoben.ac.at)

used in 2D-electronics and nanomechanics<sup>37,38</sup>. Currently, minerals such as kaolinite and montmorillonite are utilized in the biomedical, automotive, and aerospace industries for their biocompatibility, mechanical strength, thermal stability, and sustainability<sup>36,39–43</sup>. 2D phyllosilicates also show promise for energy storage applications, as in “blue batteries”<sup>44,45</sup>. They also provide insights into geological processes and past environments, including those on Mars, where their presence suggests ancient hydrological activity and potential habitability<sup>46–48</sup>.

While phyllosilicates are being researched in many different fields of science and have a number of applications, their potential as 2D magnets has been largely overlooked. While there has been extensive research on magnetism in bulk phyllosilicates<sup>49–53</sup>, a direct observation of magnetic domain structure within this mineral class remained elusive until now.

This article reports on the visualization of magnetic domains and layer-dependent magnetic ordering in phyllosilicates. Using a nanometer-sized superconducting quantum interference device (SQUID) to perform scanning SQUID microscopy (SSM)<sup>54</sup>, we directly map the stray magnetic fields above a single crystalline flake of annite, a Fe-end member of the mica family.

## Results and discussion

### Long-range magnetic ordering and imaging of the hysteresis loops in 2D flakes of annite

Annite ( $\text{KFe}_3^{2+}(\text{AlSi})_3\text{O}_{10}(\text{OH})_2$ ) belongs to the class of 2:1 layered silicates. These minerals consist of M-(O, OH) octahedra flanked by two inward-facing sheets of linked T-O tetrahedra, as illustrated in Fig. 1a. Relaxed structure obtained from ab-initio calculations is presented in Supplementary

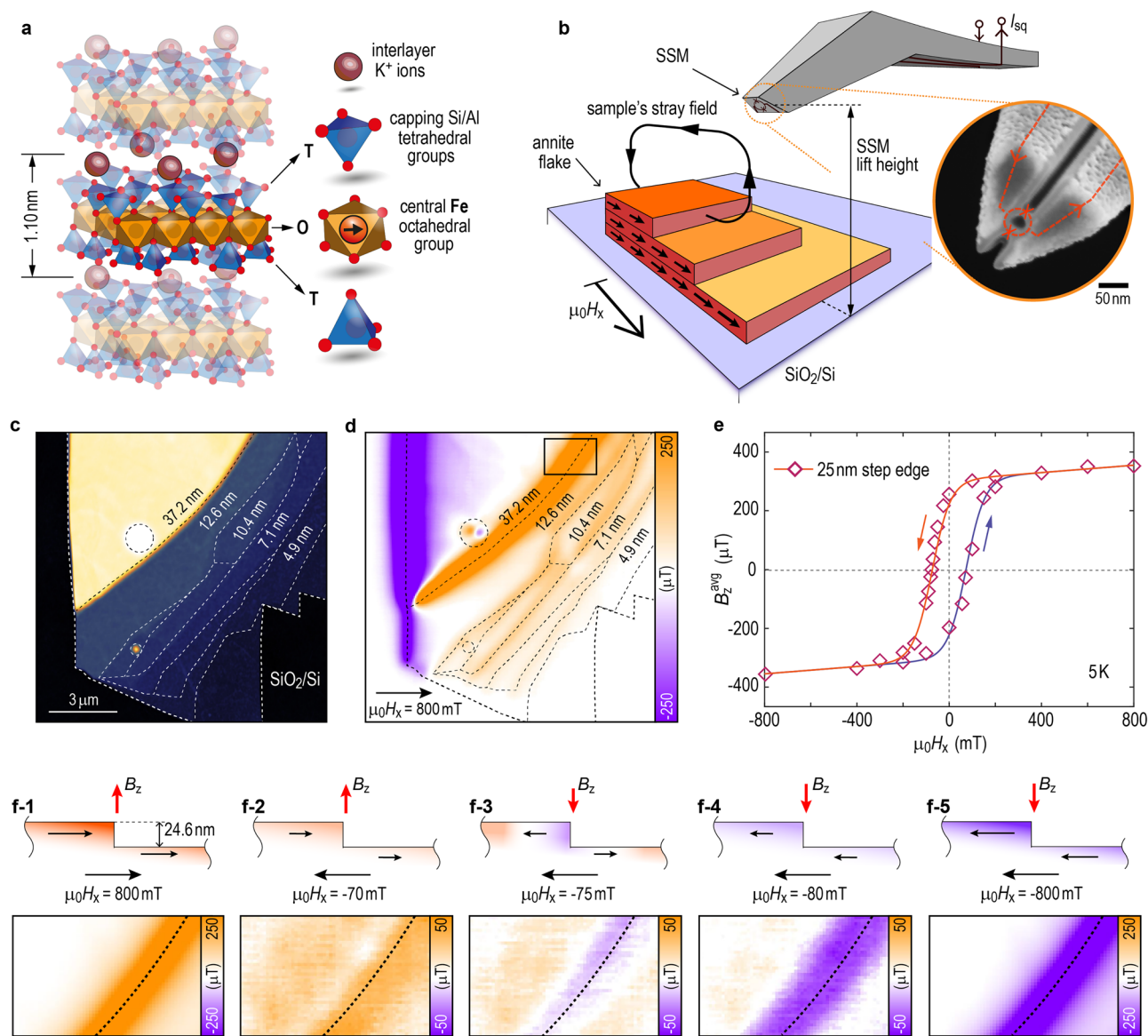


**Fig. 1 | Direct observation of long-range magnetic ordering in 2D annite.**

**a** Illustration (to scale, based on ab-initio calculations) of annite layer structure, highlighting the layer thickness, and the basic T-O-T building blocks: central octahedral groups, capping tetrahedral groups, and interlayer ions. The core Fe ion in the center of the octahedron is illustrated by a red circle and the arrow denotes the spin and the preferred in-plane orientation. **b** Schematic of the scanning SQUID microscopy experiment, illustrating fully in-plane polarized sample by the external field (left), and the scanning electron micrograph of the scanning SQUID sensor (right); dashed lines indicate the SQUID circuit. **c** AFM overview of the sample.

Dashed lines mark the atomic step transitions. Dashed circles mark trapped impurities between annite and  $\text{SiO}_2$  substrate. **d**  $B_z(x, y)$  map corresponding to the same area as in (c), under an external field of  $\mu_0 H_x = 800$  mT. **e** Magnetic hysteresis loop of the sample's stray magnetic field as a function of  $\mu_0 H_x$ , extracted from the area indicated by the solid rectangle in (d). (f1–5)  $B_z(x, y)$  maps of the marked area in (d) for selected  $\mu_0 H_x$  values from the down field sweep. Dashed lines indicate the topographic step edge. Above each sub-panel in (f1–5) a sketch of the sample's cross-section is shown, illustrating the magnetization direction along the x-axis, the applied field  $\mu_0 H_x$ , and sample's stray field  $B_z$ .

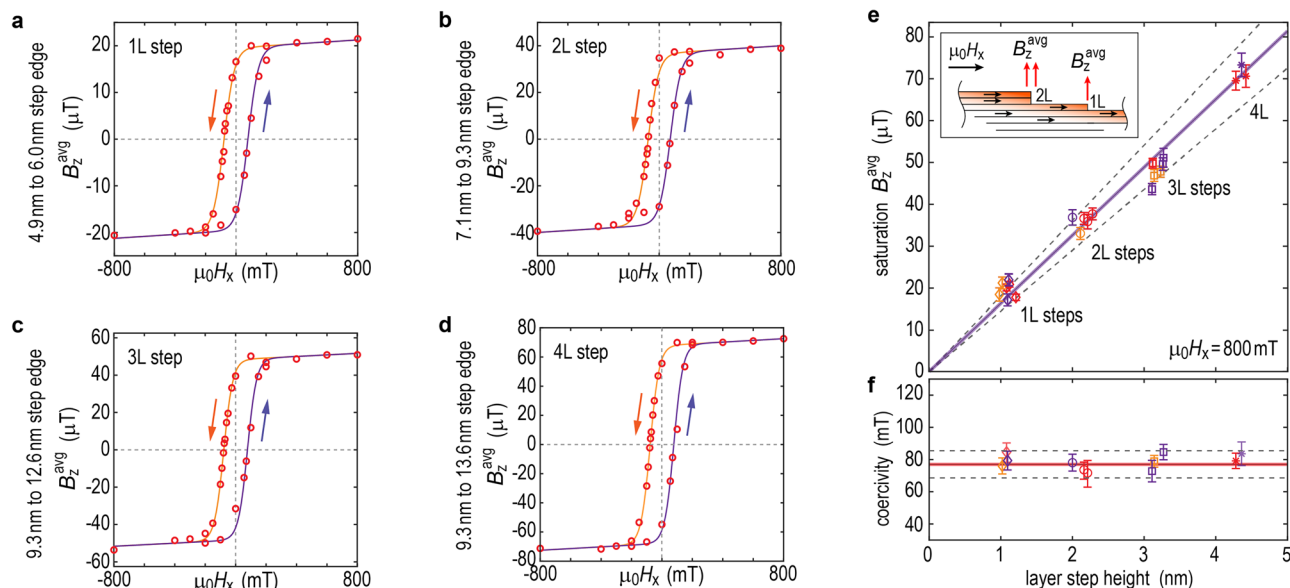


**Fig. 2 | Layer-dependent properties of the hysteresis loops.** a–d Examples of the extracted hysteresis loops from the  $B_z^{\text{avg}}(\mu_0 H_x)$  reconstructed from the different step edges, ranging from one to four monolayers within a step edge. Circles represent the extracted experimental values, while the solid lines are the best hysteresis fits (see Methods). The number of layers (L) for each step and the total flake thickness above and below the step edge is indicated in each sub-panel. e The  $B_z^{\text{avg}}$  for various step heights is plotted as a function of the layer step height when the flake is close to saturation ( $\mu_0 H_x = 800$  mT). Inset of e illustrates cross-section and the  $B_z^{\text{avg}}$  detected

from the different edges. f Coercivity as a function of the layer step height. Solid lines in (e, f) represent the mean fit through all the data points, with dashed lines indicating standard deviation. In e the fit is fixed also to the origin point. In e and f colors of the symbols indicate the different sample regions, while diamonds indicate 1L steps, circles 2L steps, squares 3L steps and stars 4L steps. Error bars in (e) and (f) demonstrate the standard deviation in  $B_z^{\text{avg}}$ , as measurements were recorded on multiple spots along the steps.

Fig. 1. In the case of annite, the central octahedral ion sites in these octahedral sheets are almost completely occupied by Fe, while the T sites are primarily filled by Si and Al<sup>55</sup>. The central Fe cations are coordinated to four oxygen atoms and two adjacent hydroxyl groups. The proximity and alignment of Fe cations within the octahedral sheets, layer separation, and the oxidation state of Fe strongly impact long-range ordering<sup>56–58</sup>. In the case of annite, a dominant A-type in-plane layer-by-layer anti-ferromagnetic behavior is observed at low temperatures<sup>55,59</sup>. The silicate double layer contains  $\text{AlO}_4$  tetrahedral groups, maintaining an Al to Si atom ratio close to 1:3. Larger ionic species, mainly potassium (K), are located between the 2:1 sheets, to maintain stoichiometric neutrality by compensating for the electron deficit from  $\text{Al}^{3+}$  substituting  $\text{Si}^{4+60,61}$ .

2D flakes of annite were mechanically exfoliated and transferred onto Si/SiO<sub>2</sub> via a dry deterministic transfer method. Due to the high crystallinity of the starting bulk annite mineral specimens (specimen number M42126.1 - mineral collection of the Royal Ontario Museum, Canada), the resulting flake exhibited a large uniform area and monolayer terraces with thicknesses down to a few layers.

To locally probe the magnetic order of 2D annite flakes, we image the out-of-plane component of their stray magnetic field  $B_z$ . All the reported SSM experiments have been conducted at a fixed temperature of  $\sim 5$  K. We scan a SQUID-on-lever probe<sup>54</sup>, illustrated in Fig. 1b, in a plane 150 nm above the sample surface. In addition to measuring  $B_z$ , we also measure  $B_z^{\text{ac}} \propto dB_z/dz$  by oscillating the sample by a few nm in the z-direction and demodulating the SQUID response at the oscillation frequency.  $B_z^{\text{ac}}$  yields higher spatial resolution and reduced background noise compared to  $B_z$ <sup>54</sup>. Figure 1c displays an atomic force microscopy (AFM) image of the examined sample. The presence of varying thicknesses within a single flake enables to observation evolution of the magnetic behavior relative to the number of layers (1L = 1.10 nm). Additional information on layer height estimates and surface roughness is provided in Supplementary Fig. 2.

For the SSM experiment presented in Fig. 1d–f, we apply an in-plane external magnetic field of  $\mu_0 H_x = 800$  mT in order to saturate the magnetization of the flake in the direction parallel to the sample's basal plane (see

Methods). The resulting  $B_z(x, y)$  is shown in Fig. 1d. The recorded signal represents the sample's out-of-plane stray magnetic field that originates predominantly from the edges (dotted line in Fig. 1d) perpendicular to the in-plane polarization. From the observed signal, it is evident that with the applied in-plane external magnetic field, the entire sample is polarized accordingly. The observed bubbles (denoted by dashed circles in Fig. 1c, d) are identified as trapped impurities between the substrate and the annite layer. These features induce localized strain and cause the basal plane of the flake to deviate from the substrate plane, consequently resulting in observed dipole-like stray fields localized near the bubbles. More information on these features is provided in Supplementary Fig. 3.

To investigate the process of magnetic reversal in 2D annite flake, we subsequently sweep down from 800 mT to  $-800$  mT in 18 discrete steps. At each  $\mu_0 H_x$ , we map  $B_z(x, y)$  above the sample. Local magnetic hysteresis loops are obtained by averaging the stray field above a particular area of the sample. By averaging the stray field above particular step edges, we can infer the magnetic behavior of the layers ending at that step. Figure 1e provides an example of the reconstructed hysteresis of  $B_z^{\text{avg}}(H_x)$  from the bulk-like step-edge of the flake (25 nm step) highlighted in Fig. 1d by a solid rectangle. Magnetization reversal in this region is observed at an applied magnetic field between 75 and 80 mT. Several SSM images of the selected step-edge are shown in Fig. 1f1–f5, following a down-sweep of the external field from 800 mT to  $-800$  mT and focusing on the recorded images around the coercive field. Reversing this procedure leads to a symmetrical inversion process. Several overview SSM maps at different  $\mu_0 H_x$  are provided in Supplementary Fig. 4.

Figure 2 presents the hysteresis data generated from over 20 distinct step edges of the sample, with step heights varying from 1 to 4 monolayers (L) and total sample thicknesses ranging from 4 to 13 nm. Representative hysteresis loops from 1L to 4L steps are shown in Fig. 2a–d. We observe that the saturation of  $B_z^{\text{avg}}$  increases linearly with the number of mono-layer steps (Fig. 2e), which demonstrates that the magnetization in these materials (magnetic moment/volume) appears to be constant from a few monolayers to bulk. The saturation values are extracted from the SSM maps measured at



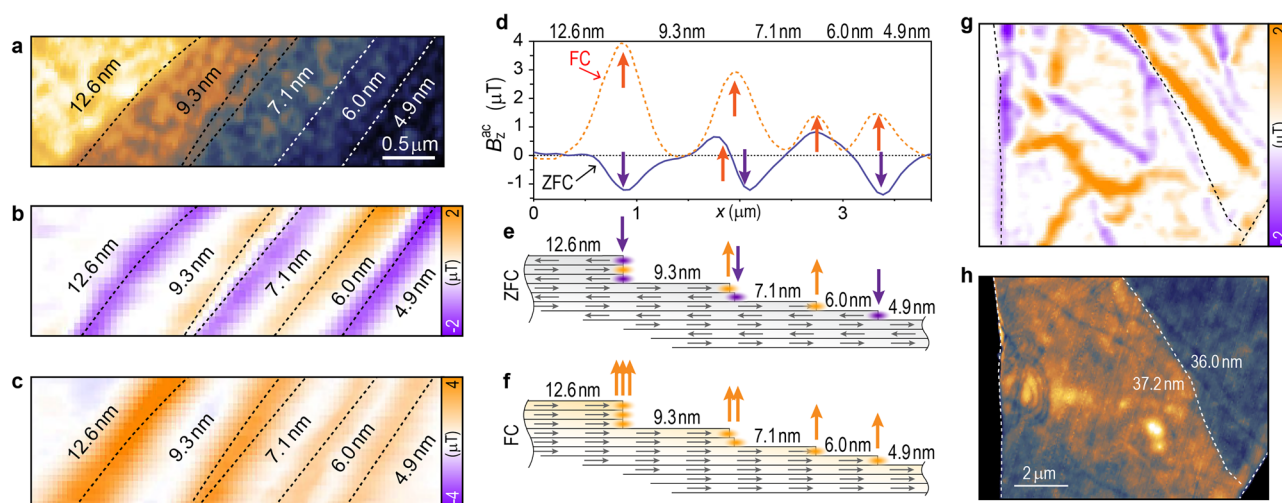


**Fig. 3 | Zero field-cooling versus field-cooling magnetic ordering.** **a** AFM image of a region with nearby flake steps, featuring 1L, 2L and 3L steps. **b**  $B_z^{\text{ac}}(x, y)$  map of the same region after zero-field-cooling from 60 K down to ~5 K. **c**  $B_z^{\text{ac}}(x, y)$  map after field-cooling with  $\mu_0 H_x = 100$  mT from 60 K to ~5 K. Prior to scanning, external field was swept back to  $\mu_0 H_x = 0$  mT. **d** Comparison of the  $B_z^{\text{ac}}$  signal considering the

cross-sections through the middle of **b** and **c** respectively. Arrows indicate the direction of the detected stray field. **e**, **f** schematic cross-sections depicting the probable spin configuration in **b** and **c**, respectively. **g**  $B_z^{\text{ac}}(x, y)$  map of a thicker region of the sample under zero-field-cooled conditions. Dashed lines indicate flake and step edges. **h** AFM image of the same area as in (**g**).

an in-plane applied external field of 800 mT. We observed that the layers beneath the step do not contribute to the measured magnetic signal, as a consequence of the fully in-plane polarized sample.

Coercivity appears to be independent of the number of layers in the probed sample thickness range (Fig. 2f), consistently measuring at  $(79 \pm 6)$  mT. This value is consistent with the bulk measurements performed at ~5.7 K (explained later in section on bulk response), indicating that layer thickness does not have an influence on the coercivity in the case of the fully saturated in-plane magnetization loops. The thickness dependent saturation of the stray field  $B_z^{\text{avg}}$  and coercivity up to 37.2 nm of total flake thickness (about 34 L), saturation of the  $B_z^{\text{avg}}$  as a function of the total flake thickness, and response of the flakes below 4.9 nm thickness are provided in the Supplementary Figs. 5 and 6.

### Intrinsic in-plane interlayer antiferromagnetic order in annite

Contrary to a fully saturated case, if annite is heated above the critical ordering temperature ( $T_c$ ) and let to cool down without any external field present, we observe a characteristic signature of the in-plane layered antiferromagnetic ordering. Figure 3 illustrates the distinct differences observed under field-cooled (FC) and zero-field-cooled (ZFC) conditions, focusing on the set of mono-, bi-, and tri-layer terraces (Fig. 3a). In the ZFC condition, the stray fields on the terraces alternate in direction, exhibiting both upward and downward orientations (Fig. 3b). For the FC conditions, the field of  $\mu_0 H_x = 100$  mT was applied during the cooling and imaging was done without the applied field. In this case, the stray fields consistently align in a single direction (Fig. 3c) dictated by the direction of the external field applied during the cool-down.

Figure 3 shows maps of  $B_z^{\text{ac}}(x, y)$ , which provides a more sensitive measure of small spatial features than  $B_z(x, y)$  (see Methods). A cross-section of  $B_z^{\text{ac}}(x, y)$  is presented in Fig. 3d. In the ZFC case, the peak intensity of the signal that correlates with the edges oscillates between approximately  $\pm 1 \mu\text{T}$ , regardless of the number of atomic steps. In the FC case, only positive peak values are observed, and the intensity linearly correlates with the number of the atomic steps. This discrepancy between the ZFC and FC observed in the SSM images can be explained if we assume that the sample orders as an in-plane interlayer antiferromagnet without the presence of the external field. This is supported by a previous Moessbauer spectroscopy study<sup>59</sup> of bulk annite. The observed stray field in the ZFC case originates from the unpaired mono-layers. Corresponding schematics of the sample cross-sections are presented in Fig. 3e, f, also illustrating the origin of the

magnetic dipoles. Furthermore, Supplementary Fig. 7 provides an example of a sample region with a predominant even number of layers on the terraces and a comparison between stray fields from 2L and 4L steps. For the sharp even number of monolayer steps and even number of layered terraces, we have observed only a weak stray field under ZFC conditions, and a clear layer-dependent signal in the FC case.

In the thicker part of the sample, we observe the formation of complex field patterns that indicate the existence of multiple magnetic domains when the sample is allowed to self-magnetize - ZFC case (Fig. 3g). The domain formation appears to be largely independent of topographical features (Fig. 3h). We hypothesize that local disorder, which is more prevalent in bulk-like samples due to the larger material volume, could play a role in domain formation during ZFC experiments. These disordered areas might serve as pinning sites, facilitating domain nucleation and growth. The observed domains range in size from about  $2 \mu\text{m}$ , down to 500 nm. However, due to the comparable size of the sample with the size of the larger domains, we cannot exclude that the observed domains are affected by the sample geometry. Additionally, we observed a reduction in feature size near the edges of the sample, suggesting the formation of fractal-like domain structures. This behavior is likely due to the system minimizing magneto-static energy by subdividing domains to reduce stray fields (Supplementary Fig. 8).

### Relation to the bulk magnetic response and Fe oxidation state

To establish a correlation between the findings from the magnetic imaging and bulk properties, we have probed long-range magnetic ordering using macroscopic SQUID magnetometry on the same bulk crystal that was used to produce the flake. Magnetization loops  $M(\mu_0 H)$  were recorded with the external field strength varied between  $\pm 5$  T, and within a temperature range between 2 K and 300 K. For single crystal annite, a field of 150 mT is required to initiate the spin flop transition from the antiferromagnetic (AFM) to the ferromagnetic (FM) state<sup>55</sup>. Figure 4a presents the SQUID magnetization loops measured along both in-plane (IP) and out-of-plane (OOP) directions of the applied external fields – with respect to the basal plane of the crystal at 2 K. Above 2 K, saturation of the magnetization is achieved in the IP orientation at an applied fields below 800 mT, whereas the OOP orientation does not reach saturation within the probed external field range of  $\pm 5$  T, supporting that the IP direction is the preferred axis of magnetization. A minor paramagnetic component is observed, which features an increase as a function of temperature (Supplementary Fig. 9). We hypothesize that the

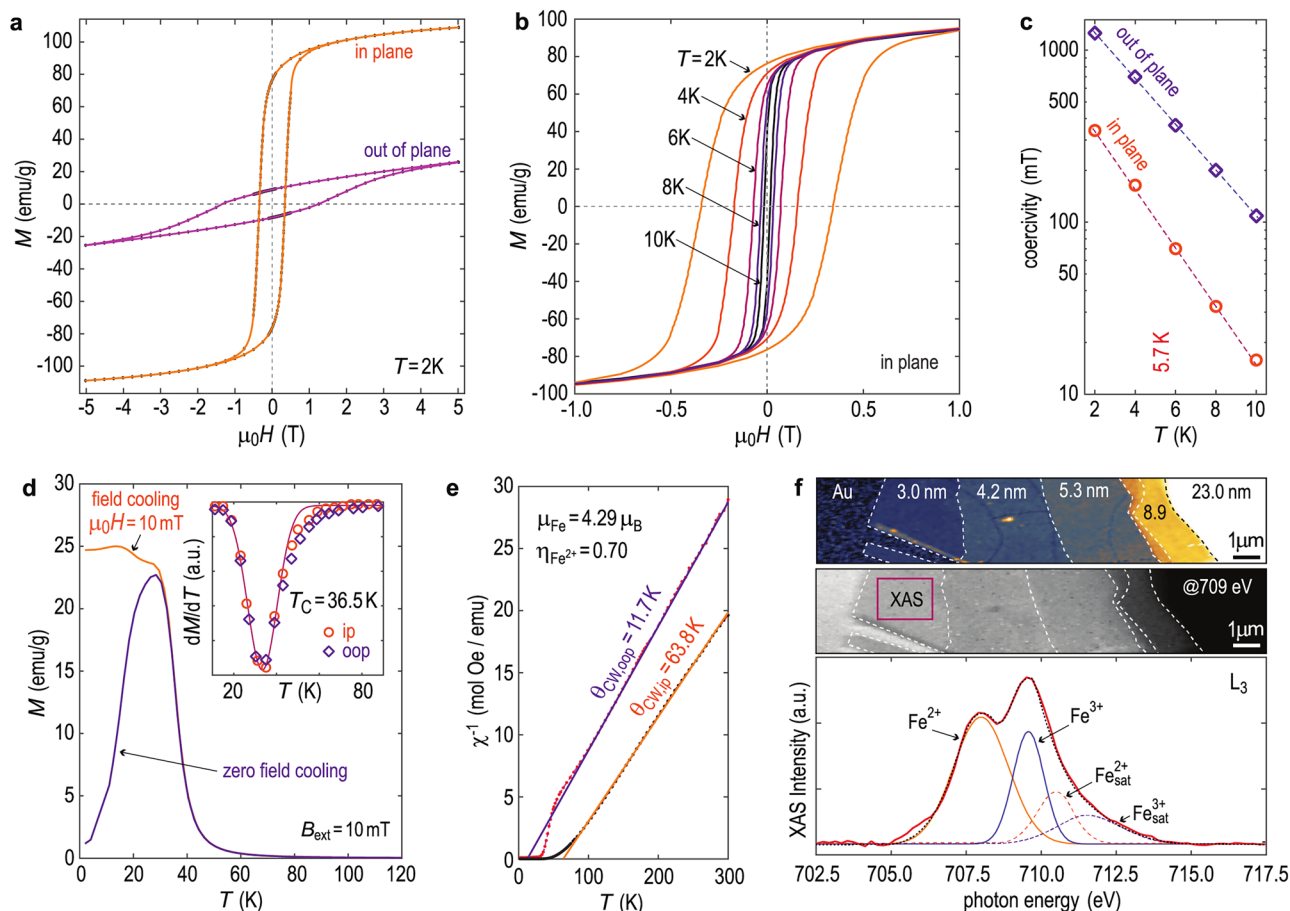


**Fig. 4 | SQUID of the bulk annite and XAS of the thin films.** **a** Hysteresis loops (at 2 K) of a bulk single-crystalline piece of annite. The loops for the in- and out-of-plane applied external field are referred with respect to the basal/cleavage plane of the sample. **b** Hysteresis loops in the case of the in-plane applied external field, at several temperatures ranging from 2 K to 10 K. **c** Coercivity as a function of the temperature (semi-log scale). Circles represent in-plane and diamonds out-of-plane applied external fields, dashed lines are exponential fits. **d** ZFC (purple) and FC (orange) curves of bulk annite crystal. For the FC-case, 10 mT of the external in-plane field was applied. Inset of **d** present normalized  $dM/dT$  values as a function of  $T$ . Circles denote the values obtained from the FC-ip curves, and diamonds are obtained from the FC-oop curves. A solid line represents a Gaussian fit. **e** Inverse susceptibility as a function of  $T$ , considering in-plane and out-of-plane FC curve. Solid line represents

the fit with respect to Curie-Weiss law, and is fitted to the range of 100–300 K.  $\theta_{CW}$  value is indicated along the line, extracted moment per iron atom and the estimated ratio of the 2+ versus 3+ oxidation states of iron are also indicated. **f** XAS data extracted from XPEEM imaging. The top panel presents an AFM image of the sample, indicating number of mono-layers. The middle panel presents the X-ray absorption image obtained at 709 eV energy. Dashed lines indicate layer-steps. Bottom panel presents X-ray absorption spectrum across the Fe  $L_3$  edge (solid red line) with individual Gaussian fits for the main and the satellite peaks that correspond to the 2+ and 3+ oxidation states of Fe. A cumulative fit is presented by the dotted line. The spectrum was taken from the 3.0 nm thin flake, with the ROI indicated by the red rectangle in the middle panel.

paramagnetic component originates from the potentially disordered regions in the bulk crystal.

Figure 4b shows a temperature evolution of the IP  $M(\mu_0 H)$  loops, between 2 K and 10 K. Magnetization loops recorded in the OOP configuration are provided in Supplementary Fig. 10. Observed temperature dependent coercivity for both IP and OOP  $M(\mu_0 H)$  loops is presented in Fig. 4c. From here, we can estimate that sample temperature in the magnetic imaging study was at about 5.7 K, assuming that the coercivity is the same in both bulk and thin films.

$T_C$  of the examined bulk annite sample and the behavior in the paramagnetic regime were determined from the bulk FC and ZFC experiments. The  $M(T)$  curves, provided in Fig. 4d, were obtained by cooling down from 300 K to 2 K, with applied IP/OOP 10 mT in the FC cases. From the global minima of the first derivative ( $dM/dT$ ) we observe the same  $T_C$  of 36.5 K for both IP and OOP applied fields.

By extracting the inverse of the susceptibility ( $\chi^{-1}$ ) from the  $M(T)$  curves (Fig. 4e), we see that the Curie-Weiss (CW) paramagnetism<sup>62</sup> well describes the behavior of annite above  $\sim 100$  K. At low temperatures, an upturn observed in ( $\chi^{-1}$ ) is attributed to onset of magnetic ordering and/or

the presence of additional magnetic contributions. Knowing the volume and the composition of the sample, from the slope of the CW fit, we obtain that Fe ions carry a local moment of  $4.29 \mu_B$ . This indicates the mixture of  $Fe^{2+}$  and  $Fe^{3+}$  states<sup>56,63</sup>. The inverse of the susceptibility slope implies to the mixture between 2+ and 3+ oxidation states of iron, with  $\eta_{Fe}^{2+} = (0.7 \pm 0.2)$ . The value  $\eta_{Fe}^{2+}$  presents a fraction of the Fe in the 2+ oxidation state.

The point where the CW fit cuts the temperature axis refers to the  $\theta_{CW}$ , or the Curie-Weiss temperature. From the CW fits to the  $M(T)$  in the range above 100 K, we obtain  $\theta_{CW,IP} = 63.8$  K and  $\theta_{CW,OOP} = 11.7$  K from the IP and OOP FC curves, respectively. The discrepancy between  $\theta_{CW}$  and  $T_C$  values obtained from the  $dM/dT$  minima, are referred to as the two- $T_C$  problem<sup>55</sup>. This implies to a complex behavior of magnetic phyllosilicates in the range where inter-layer and intra-layer coupling mechanisms compete. For the IP-case, below 36.5 K, the intra-layer magnetic coupling is stronger than the inter-layer coupling, and the ordering observed in the SSM experiments prevails. As the temperature rises above  $T_C$ , the inter-layer magnetic interactions weaken, leading to the decoupling of the magnetic behavior of the layers. In this regime, the layers exhibit superparamagnetic

behavior due to the increased thermal fluctuations. At temperatures above 63.8 K, the intra-layer magnetic interactions also begin to weaken, resulting in a breakdown of the remaining magnetic order within each layer, resulting in a paramagnetic state. We hypothesize that this behavior persists in the 2D limit, as SSM and SQUID measurements indicate that layers interact weakly.

Below  $T_C$ , the  $dM/dT$  curves reveal a configuration-dependent behavior; the in-plane measurements exhibit a second local minimum near 20.8 K, absent in the out-of-plane (OOP) data (Supplementary Fig. 11). This feature likely reflects a secondary magnetic transition associated with  $\text{Fe}^{3+}$  dominated regions exhibiting a lower  $T_C$ <sup>49,56</sup>. In addition to  $T_C$ , the temperature derivative of the ZFC magnetization curve exhibits a global minima at 34.7 K, referred to be the Néel temperature ( $T_N$ ) (Supplementary Fig. 11).

To confirm that the mixed oxidation state of Fe is preserved also in the 2D limit, we have performed X-ray absorption spectroscopy (XAS) on 2D flakes, focusing on the  $\text{Fe } L_3$  edge, by means of photoemission electron microscopy (PEEM)<sup>64</sup>. Figure 4f presents the absorption spectrum corresponding to the region of interest (ROI) highlighted in the top of the panel (also showing XAS absorption map and the correlated AFM topography). The analysis reveals a mixed valence state of iron, characterized by significant proportions of  $\text{Fe}^{2+}$  and  $\text{Fe}^{3+}$  (Supplementary Fig. 12). In the thin flakes, approximately  $\eta_{\text{Fe}}^{2+} = 0.55$  of the iron exists in the  $\text{Fe}^{2+}$  state. The discrepancy to the data obtained from the CW fit could be attributed to a combination of the close proximity to the metallic substrate needed for the PEEM experiment and potential damage by the X-ray beam that could cause a transition from a  $2+$  to a  $3+$  state. It was reported that the mixed valence state and the competing  $\text{Fe}^{2+}$ - $\text{Fe}^{2+}$  versus  $\text{Fe}^{2+}$ - $\text{Fe}^{3+}$  interactions could allow for tuning of the  $T_C$ , even potentially reaching the room temperature<sup>32,56</sup>.

## Conclusion

Considering the entire mineral class of phyllosilicates, our SSM experiments on exfoliated single-crystalline flakes of annite (fully Fe-substituted mica) provide the first direct imaging of long-range net magnetic ordering and its layer dependence in the 2D limit. We have observed that in the presence of the external in-plane magnetic field the films order ferromagnetically, while intrinsically (without the external fields), the films order as A-type in-plane layer-by-layer antiferromagnets.

As 2D magnetic micas are fully air-stable, large band-gap, and high- $k$  vdW insulators, there are many opportunities to consider their integration into magnetoresistive tunneling junctions, magnetic random access memories, spin transistors, and nano-scaled sensors. Therefore, these 2D magnetic insulators could potentially be a core functional building blocks for computing in memory technologies. Since many phyllosilicates are biocompatible and bio-degradable, further understanding and engineering magnetism in this material class, especially at the 2D limit, could open avenues in bio-technologies, as targeted drug delivery and in-vivo bio-sensing.

## Methods

### Sample preparation

A 2D flake of annite was prepared through micromechanical exfoliation using sticky tape (Nitto Denko ELP BT150ECM). The process involved repeatedly peeling the material against two pieces of tape, following a transfer either to PDMS stamps or directly to  $\text{Si}/\text{SiO}_2$  chips (with a 300 nm wet oxide layer). In the case of gold-coated Si chips, PDMS stamps were used to prevent partial peeling of the gold film from the substrate. An optical microscope was initially used to identify the 2D flakes with sufficiently thin regions.

### AFM measurements

Ambient AFM pre-characterization was conducted using a Horiba /AIST-NT Omegascope AFM system. NuNano SPARK 350 Pt probes were used, with a spring constant of 42 N/m, a resonant frequency of 350 kHz, and a tip radius of 30 nm. Open-source software Gwyddion v2.56 was used to process topography images, and thickness was measured by the bent step function fitting the selected cross-section height profiles. Commonly, zero-order line correction was applied, followed by the tree point averaging of the substrate plane with respect to a single largest terrace.

## SSM

The SQUID-on-lever scanning probe is fabricated by sputtering Nb on an AFM cantilever and patterning its apex via focused-ion-beam milling, as described by Wyss et al.<sup>54</sup>. The sensor is operated at 4.2 K in a semi-voltage biased circuit, in which the current response  $I_{\text{sq}}$  is measured by a series SQUID array amplifier (Magnicon). By measuring the quantum interference pattern of the SQUID sensor, we determine an effective diameter of 140 nm. The sensor has an AC magnetic field sensitivity exceeding  $S_B^{1/2} = 1 \mu\text{T Hz}^{-1/2}$  in the white-noise regime.

SSM is carried out in a custom-built scanning probe microscope operating under high vacuum within a  $^4\text{He}$  cryostat. Since  $I_{\text{SQUID}}$  is proportional to magnetic flux, this response provides a measure of the local magnetic field threading through the SQUID loop. The sensor is calibrated by measuring the response of  $I_{\text{SQUID}}$  as a function of an out-of-plane applied magnetic field  $\mu_0 H_z$ . During imaging, the out-of-plane field was adjusted between 10–20 mT to optimize the SQUID sensor's field-dependent sensitivity for detecting the sample's stray field. The pixel size of the magnetic images varies from 35 to 65 nm and the acquisition time is around 0.2 s/pixel. The time constant used for the  $B_z^{\text{ac}}$  scans is  $\tau \approx 150$  ms. By scanning the sample using a scanning probe controller (Specs) and piezoelectric actuators (Attocube) at a constant tip-sample spacing of 150 nm, we map  $B_z(x, y)$  and  $B_z^{\text{ac}}(x, y)$  in a plane above the sample.  $B_z^{\text{ac}} \propto dB_z/dz$  is measured by oscillating the sample by less than 10 nm at 78 Hz using a piezoelectric actuator and demodulating the SQUID response at the oscillation frequency. Due to spectral filtering and the higher spatial resolution characteristic of measuring a magnetic field derivative<sup>65</sup>, the resulting signal contains less noise than  $B_z$ . Spatial resolution is limited by the tip-sample spacing and by the effective diameter of the SQUID loop to approximately 150 nm. Note that the axis of the SQUID is tilted by  $10^\circ$  with respect to the  $z$ -axis, because the SSM is scanned in a standard AFM configuration to enable easy approach the sensor tip without touching the rest of the cantilever body. As a result, both  $B_z(x, y)$  and  $B_z^{\text{ac}}(x, y)$  are measured with a  $10^\circ$  tilt with respect to the  $z$ -axis.

SSM maps were recorded from 800 mT to -800 mT in 18 steps, since the hysteresis loops reach magnetic saturation around  $\mu_0 H_z = -300$  mT. The number of recorded SSM maps was reduced in the range between  $\pm 400$  mT and  $\pm 800$  mT.

### SSM hysteresis reconstruction and fitting

From a sequence of the SSM maps at the different applied external fields ( $\mu_0 H_x$ ), first a drift compensation between each SSM map is corrected for, followed by a correlation to the pre-recorded high-resolution topography map of the sample. Next, a rectangular region of interest (ROI) containing only a single step-edge of interest is selected, having the edges predominantly perpendicular to the  $x$  axis of the ROI. For each row of the ROI of the SSM map (at a fixed  $\mu_0 H_x$ ) the peak  $B_z$  value is taken. These are averaged over the ROI's rows, yielding  $B_z^{\text{avg}}(\mu_0 H_x)$  for the selected edge. The hysteresis loop is then reconstructed by repeating the process for the same ROI at the different external fields.

Fitting of the hysteresis loops extracted from the SSM experiments was used for relative comparison of the saturation values with respect to the ferromagnetic component of the signal and for extracting the coercivity values. For these, smoothed step functions were fitted to each branch of the loop simultaneously. A linear, paramagnetic, component was also added to the fit. Four fitting parameters were used: saturation of the magnetization, coercivity, spreading of the loop, and the paramagnetic slope. The loop parameters were fixed for both branches. If the forward and the backward branches of the loop are fitted separately, only minor deviation in the extracted parameters is observed.

### Bulk SQUID magnetometry

Bulk SQUID magnetometry: Long-range magnetic ordering of the bulk crystal was probed using SQUID MPMS XL from Quantum Design. The annite crystal was cut to dimensions of  $4 \times 4 \text{ mm}^2$ , and mounted on  $\text{Si}/\text{SiO}_2$  chip and placed inside the plastic straw holder to be able to measure both in-



plane and out-of-plane  $M(\mu_0 H)$  curves at different temperatures using the same piece of sample. The measured magnetic moment was normalized to the weight of the measured annite crystal, and the diamagnetic contribution of the Si substrate was derived from the high-field magnetization curves at 300 K and subtracted from all magnetization curves.  $M(T)$  curves were recorded in IP and OOP configurations. The sample was cooled down zero field (nominally, after the magnet reset), i.e., residual field  $\sim -0.2$  mT. Then, at a low temperature 10 mT field is applied, followed by  $M(T)$  measurements while warming. The comparison with the FC gives the range where the sample behaves hysteretically. Temperature-dependent static magnetic susceptibility ( $\chi$ ) and its inverse ( $\chi^{-1}$ ) were extracted from  $M(T)$  measurements performed under a small, constant magnetic field of 10 mT. The susceptibility values presented reflect the total magnetic response measured under the experimental conditions without any explicit paramagnetic subtraction.

### X-ray Absorption spectroscopy

X-ray absorption spectroscopy (XAS) measurements were conducted utilizing the SPEEM end-station of UE49-PGMA beamline at the BESSY II synchrotron radiation facility<sup>64</sup>. 2D flakes of annite were deposited onto gold-coated (50 nm) silicon chips for analysis. Both images and spectra were obtained under linear polarized X-rays at a sample temperature of 40 K.

### Data availability

The data that support the findings of this study are available from the corresponding author upon reasonable request. The set of raw data which corresponds to the figures in the manuscript (where applicable) is also available via: <https://doi.org/10.5281/zenodo.17050437>.

Received: 9 May 2025; Accepted: 29 August 2025;

Published online: 02 October 2025

### References

- Huang, B. et al. Emergent phenomena and proximity effects in two-dimensional magnets and heterostructures. *Nat. Mater.* **19**, 1276–1289 (2020).
- Mi, M. et al. Two-dimensional magnetic materials for spintronic devices. *Mater. Today Nano* **24**, 100408 (2023).
- Montblanch, A. R.-P., Barbone, M., Aharonovich, I., Atatüre, M. & Ferrari, A. C. Layered materials as a platform for quantum technologies. *Nat. Nanotechnol.* **18**, 555–571 (2023).
- Hao, Q. et al. 2d magnetic heterostructures and emergent spintronic devices. *Adv. Electron. Mater.* **8**, 2200164 (2022).
- Wang, Q. H. et al. The magnetic genome of two-dimensional van der Waals materials. *ACS Nano* **16**, 6960–7079 (2022).
- Li, H., Ruan, S. & Zeng, Y.-J. Intrinsic van der Waals magnetic materials from bulk to the 2d limit: new frontiers of spintronics. *Adv. Mater.* **31**, 1900065 (2019).
- Song, T. et al. Giant tunneling magnetoresistance in spin-filter van der Waals heterostructures. *Science* **360**, 1214–1218 (2018).
- Chu, J. et al. 2d polarized materials: ferromagnetic, ferrovalley, ferroelectric materials, and related heterostructures. *Adv. Mater.* **33**, 2004469 (2021).
- Mak, K. F., Shan, J. & Ralph, D. C. Probing and controlling magnetic states in 2d layered magnetic materials. *Nat. Rev. Phys.* **1**, 646–661 (2019).
- Lee, J.-U. et al. Ising-type magnetic ordering in atomically thin fep3s. *Nano Lett.* **16**, 7433–7438 (2016).
- Lee, Y. et al. Giant magnetic anisotropy in the atomically thin van der Waals antiferromagnet fep3s. *Adv. Electron. Mater.* **9**, 2200650 (2023).
- Son, J. et al. Air-stable and layer-dependent ferromagnetism in atomically thin van der Waals CrPS4. *ACS Nano* **15**, 16904–16912 (2021).
- Lee, K. et al. Magnetic order and symmetry in the 2d semiconductor CrSbR. *Nano Lett.* **21**, 3511–3517 (2021).
- Huang, B. et al. Layer-dependent ferromagnetism in a van der Waals crystal down to the monolayer limit. *Nature* **546**, 270–273 (2017).
- Gong, C. et al. Discovery of intrinsic ferromagnetism in two-dimensional van der Waals crystals. *Nature* **546**, 265–269 (2017).
- May, A. F. et al. Ferromagnetism near room temperature in the cleavable van der Waals crystal Fe5GeTe2. *ACS Nano* **13**, 4436–4442 (2019).
- Li, D., Li, S., Zhong, C. & He, J. Tuning magnetism at the two-dimensional limit: A theoretical perspective. *Nanoscale* **13**, 19812–19827 (2021).
- Jiang, S., Shan, J. & Mak, K. F. Electric-field switching of two-dimensional van der Waals magnets. *Nat. Mater.* **17**, 406–410 (2018).
- Yan, H. et al. Electric-field-controlled antiferromagnetic spintronic devices. *Adv. Mater.* **32**, 1905603 (2020).
- Zhang, R.-Z., Zhang, Y.-Y. & Du, S.-X. Thickness-dependent magnetic order and phase transition in v5s8. *Chin. Phys. B* **29**, 077504 (2020).
- van Uijen, C., Frikkie, E. & de Wijn, H. Neutron scattering study of magnetic ordering in the double-layer antiferromagnet k 3 mn 2 f 7. *Phys. Rev. B* **19**, 509 (1979).
- Yusuf, S. & Kumar, A. Neutron scattering of advanced magnetic materials. *Appl. Phys. Rev.* **4**, 031303 (2017).
- Seemann, K. M. & Kronast, F. Artificial magnetic domains by interlayer coupling in an in-plane/perpendicular-to-plane magnetic bilayer system. *Phys. Rev. B* **111**, 174439 (2025).
- Zhang, T. et al. Degradation chemistry and kinetic stabilization of magnetic cri3. *J. Am. Chem. Soc.* **144**, 5295–5303 (2022).
- Xu, H. et al. Recent advances in two-dimensional van der Waals magnets. *Microstructures* **2**, 2022011 (2022).
- Zhang, F. et al. Monolayer vanadium-doped tungsten disulfide: a room-temperature dilute magnetic semiconductor. *Adv. Sci.* **7**, 2001174 (2020).
- Fu, S. et al. Enabling room temperature ferromagnetism in monolayer MoS2 via in situ iron-doping. *Nat. Commun.* **11**, 2034 (2020).
- Wang, Y., Li, S. & Yi, J. Electronic and magnetic properties of Co doped MoS2 monolayer. *Sci. Rep.* **6**, 24153 (2016).
- Zhong, J.-Q. & Freund, H.-J. Two-dimensional ultrathin silica films. *Chem. Rev.* **122**, 11172–11246 (2022).
- Peschel, G. et al. Growth and structure of ultrathin iron silicate and iron germanate films. *J. Phys. Chem. C* **128**, 19423–19435 (2024).
- Frisenda, R., Niu, Y., Gant, P., Muñoz, M. & Castellanos-Gomez, A. Naturally occurring van der Waals materials. *npj 2D Mater. Appl.* **4**, 38 (2020).
- Matković, A. et al. Iron-rich talc as air-stable platform for magnetic two-dimensional materials. *npj 2D Mater. Appl.* **5**, 94 (2021).
- Barcelos, I. D. et al. Phyllosilicates as earth-abundant layered materials for electronics and optoelectronics: Prospects and challenges in their ultrathin limit. *J. Appl. Phys.* **134** (2023).
- de Oliveira, R. et al. Ultrathin natural biotite crystals as a dielectric layer for van der Waals heterostructure applications. *Nanotechnology* **35**, 505703 (2024).
- Pacakova, B. et al. Naturally occurring 2d semiconductor with antiferromagnetic ground state. *npj 2D Mater. Appl.* **9**, 1–8 (2025).
- Xie, W., Chen, Y. & Yang, H. Layered clay minerals in cancer therapy: recent progress and prospects. *Small* **19**, 2300842 (2023).
- Nutting, D. et al. Electrical and optical properties of transition metal dichalcogenides on talc dielectrics. *Nanoscale* **13**, 15853–15858 (2021).
- Vasić, B. et al. Two-dimensional talc as a van der Waals material for solid lubrication at the nanoscale. *Nanotechnology* **32**, 265701 (2021).
- Włodarczyk, A., Gorgoń, S., Radoń, A. & Bajdak-Rusinek, K. Magnetite nanoparticles in magnetic hyperthermia and cancer therapies: Challenges and perspectives. *Nanomaterials* **12**, 1807 (2022).
- Liu, Y. et al. All-natural phyllosilicate-polysaccharide triboelectric sensor for machine learning-assisted human motion prediction. *npj Flex. Electron.* **7**, 21 (2023).

41. Nandhini, J., Karthikeyan, E. & Rajeshkumar, S. Eco-friendly bio-nanocomposites: pioneering sustainable biomedical advancements in engineering. *Discov. Nano* **19**, 86 (2024).
42. Wu, Q., Liao, J. & Yang, H. Recent advances in kaolinite nanoclay as drug carrier for bioapplications: a review. *Adv. Sci.* **10**, 2300672 (2023).
43. Tang, Y. et al. Preparation and thermal stability of polypropylene/montmorillonite nanocomposites. *Polym. Degrad. Stab.* **82**, 127–131 (2003).
44. Lan, Y. et al. Natural clay-based materials for energy storage and conversion applications. *Adv. Sci.* **8**, 2004036 (2021).
45. Artemov, V. et al. Ultraconfined 1-nm water as nature-inspired electrolyte for blue batteries. *arXiv preprint arXiv:2410.11983* (2024).
46. Poulet, F. et al. Phyllosilicates on Mars and implications for early Martian climate. *Nature* **438**, 623–627 (2005).
47. Chevrier, V., Poulet, F. & Bibring, J.-P. Early geochemical environment of Mars as determined from thermodynamics of phyllosilicates. *Nature* **448**, 60–63 (2007).
48. Bishop, J. L. Remote detection of phyllosilicates on Mars and implications for climate and habitability. In *From habitability to life on Mars*, 37–75 (Elsevier, 2018).
49. Ballet, O. & Coey, J. Magnetic properties of sheet silicates; 2: 1-layer minerals. *Phys. Chem. Miner.* **8**, 218–229 (1982).
50. Borradaile, G. J. & Werner, T. Magnetic anisotropy of some phyllosilicates. *Tectonophysics* **235**, 223–248 (1994).
51. Richard-Plouet, M. & Vilminot, S. Ferromagnetism in talc-like cobalt-phyllosilicates. *Solid State Sci.* **1**, 381–393 (1999).
52. Coey, J., Ballet, O., Moukarika, A. & Soubeyroux, J. Magnetic properties of sheet silicates; 1: 1 layer minerals. *Phys. Chem. Miner.* **7**, 141–148 (1981).
53. Coey, J. M. D. Magnetic order in trioctahedral sheet silicates: a review. In *Proc. International Clay Conference*, Denver, 261–266 (1985).
54. Wyss, M. et al. Magnetic, thermal, and topographic imaging with a nanometer-scale squid-on-lever scanning probe. *Phys. Rev. Appl.* **17**, 034002 (2022).
55. Rancourt, D., Christie, I., Lamarche, G., Swainson, I. & Flandrois, S. Magnetism of synthetic and natural annite mica: ground state and nature of excitations in an exchange-wise two-dimensional easy-plane ferromagnet with disorder. *J. Magn. Magn. Mater.* **138**, 31–44 (1994).
56. Khan, M. Z. et al. Probing magnetic ordering in air-stable iron-rich van der Waals minerals. *Adv. Phys. Res.* **2**, 2300070 (2023).
57. Brigatti, M. F., Affronte, M., Elmi, C., Malferrari, D. & Laurora, A. Trioctahedral Fe-rich micas: Relationships between magnetic behavior and crystal chemistry. *Am. Miner.* **100**, 2231–2241 (2015).
58. Pini, S., Brigatti, M. F., Affronte, M., Malferrari, D. & Marcelli, A. Magnetic behavior of trioctahedral micas with different octahedral Fe ordering. *Phys. Chem. Miner.* **39**, 665–674 (2012).
59. Christie, I. A. *The magnetic properties of annite: A SQUID magnetometry and iron-57 Moessbauer spectroscopy study*. (University of Ottawa (Canada), 1994).
60. Mottana, A., Sassi, F. P., Thompson, J. B. & Guggenheim, S. *Micas: Crystal chemistry & metamorphic petrology*, vol. 46 (Walter de Gruyter GmbH & Co KG, 2018).
61. Franceschi, G. et al. Resolving the intrinsic short-range ordering of k<sup>+</sup> ions on cleaved muscovite mica. *Nat. Commun.* **14**, 208 (2023).
62. Mugiraneza, S. & Hallas, A. M. Tutorial: a beginner's guide to interpreting magnetic susceptibility data with the Curie-Weiss law. *Commun. Phys.* **5**, 95 (2022).
63. Zou, Y.-C. et al. Ion exchange in atomically thin clays and micas. *Nat. Mater.* **20**, 1677–1682 (2021).
64. Kronast, F. & Molina, S. V. Speem: The photoemission microscope at the dedicated microfocus pgm beamline ue49-pgma at Bessy II. *J. Large-scale Res. Facil. JLSRF* **2**, A90–A90 (2016).
65. Marchiori, E. et al. Nanoscale magnetic field imaging for 2D materials. *Nat. Rev. Phys.* **4**, 49–60 (2022).

## Acknowledgements

This work is supported by the Austrian Science Fund (FWF) under grant no. Y1298-N, and by the ERC Starting grant POL\_2D\_PHYSICS (101075821). We acknowledge support of the European Commission under H2020 FET Open grant “FIBsuperProbes” (Grant No. 892427), the SNF under Grant no. 207933, and the Canton Aargau. We acknowledge the Royal Ontario Museum (Canada) for the loan of the M42126.1 annite specimen. We thank the Helmholtz-Zentrum Berlin für Materialien und Energie for the allocation of synchrotron radiation beamtime.

## Author contributions

M.Z.K. carried out the sample preparation and AFM characterization. M.Z.K. and A.M. interpreted AFM data. O.E.P. carried out the calculations. A.V., K.B., and D.J. performed the scanning SQUID microscopy measurements. A.N. carried out bulk SQUID experiments and interpreted the data. M.Z.K., under the supervision of A.S., S.V., and F.K., carried out XAS experiments. D.K. and M.D. contributed to the initial idea and the compilation of the manuscript. M.Z.K., D.J., A.V., and K.B. compiled all the data and wrote the manuscript with the assistance of A.M. and M.P. All authors discussed the results and reviewed the manuscript.

## Competing interests

The authors declare no competing interests.

## Additional information

**Supplementary information** The online version contains supplementary material available at <https://doi.org/10.1038/s43246-025-00936-7>.

**Correspondence** and requests for materials should be addressed to Martino Poggio or Aleksandar Matković.

**Peer review information** *Communications Materials* thanks the anonymous reviewers for their contribution to the peer review of this work. A peer review file is available.

**Reprints and permissions information** is available at <http://www.nature.com/reprints>

**Publisher's note** Springer Nature remains neutral with regard to jurisdictional claims in published maps and institutional affiliations.

**Open Access** This article is licensed under a Creative Commons Attribution-NonCommercial-NoDerivatives 4.0 International License, which permits any non-commercial use, sharing, distribution and reproduction in any medium or format, as long as you give appropriate credit to the original author(s) and the source, provide a link to the Creative Commons licence, and indicate if you modified the licensed material. You do not have permission under this licence to share adapted material derived from this article or parts of it. The images or other third party material in this article are included in the article's Creative Commons licence, unless indicated otherwise in a credit line to the material. If material is not included in the article's Creative Commons licence and your intended use is not permitted by statutory regulation or exceeds the permitted use, you will need to obtain permission directly from the copyright holder. To view a copy of this licence, visit <http://creativecommons.org/licenses/by-nc-nd/4.0/>.

© The Author(s) 2025